Reconstruction of nearshore surface gravity waves from Distributed Acoustic Sensing data

Samuel Meulé[1], Julián Pelaez-Quiñones[2*], Fréderic Bouchette[3], Anthony Sladen[2], Aurélien Ponte[4], Annika Maier[5], Itzhak Lior[6], Paschal Coyle[7]

[1]Aix Marseille University, CNRS, IRD, INRAE, Coll France, CEREGE, Aix-en-Provence, France
[2]Universite Côte d'Azur, CNRS, Observatoire de la Côte d'Azur, IRD, Géoazur, Sophia Antipolis, 250 rue Albert Einstein, 06560, Valbonne, France
[3]GEOSCIENCES-Montpellier, Univ Montpellier, CNRS, Montpellier, France
[4]IFREMER, Université de Brest, CNRS, IRD, Laboratoire d'Océanographie Physique et Spatiale, IUEM, Brest, France
[5]Karlsruhe Institute of Technology, Karlsruhe, Germany
[6]Institute of Earth Sciences, The Hebrew University, Jerusalem, Israel
[7]Aix-Marseille Université, CNRS/IN2P3, CPPM, Marseille, France
[*]Now at the Department of Physics and Technology, University of Bergen, P.O. Box 7803, N-5020 Bergen, Norway

Key Points:

- A simple transfer function between DAS and a collocated pressure sensor is retrieved for surface gravity waves
- Ocean waveheights are correctly reconstructed from nearshore DAS measurements
- The signals recorded by DAS can be described from the standpoint of the linear wave theory

Corresponding author: Samuel Meulé, `meule@cerege.fr`

Abstract

Distributed Acoustic Sensing (DAS) is a photonics technology converting seafloor telecommunications and optical fiber cables into dense arrays of strain sensors, allowing to monitor various oceanic physical processes. Yet, several applications are hindered by the limited knowledge of the transfer function between geophysical variables and DAS measurements. This study investigates the quantitative relationship between surface gravity DAS-recorded wave-generated strain signals along the seafloor and the pressure at a colocated sensor. A remarkable linear correlation is found over various sea conditions allowing to reliably determine significant wave heights from DAS data. Utilizing linear wave potential theory, we derive an analytical transfer function linking cable deformation and wave kinematic parameters. This transfer function provides a first quantification of the effects related to waves and fiber responses. Our results validate DAS's potential for real-time reconstruction of the surface gravity wave spectrum over extended coastal areas. It also enables the estimation of waves hydraulic parameters at depth without the need of offshore deployments.

Plain Language Summary

Distributed Acoustic Sensing (DAS) technology converts submarine communication cables into real-time networks of thousands of seismo-acoustic sensors. The high sensitivity of DAS measurements (nano-deformation) makes the recorded signals extremely rich in information, and capable of capturing multiple oceanographic processes. Numerous applications can be envisaged such as monitoring turbidity currents, tsunamis, marine renewable energy parks, etc., and some are already in progress, including monitoring surface vessels, marine currents, cetaceans, etc. However, despite all these developments, the relationship between DAS measurements and certain key ocean variables remains poorly understood. In the littoral zone, this study aims to investigate the link between the deformation signals recorded by DAS due to wave passage at the sea surface and the pressure measured by a sensor located nearby, at the bottom. Our findings demonstrate a strong correlation under varying sea conditions. This correlation allows to reliably determine significant wave heights using DAS data. By applying a simplified theory of wave propagation, the linear wave theory, it was possible to develop an analytical transfer function that relates cable deformation to wave movement parameters. The results confirm that DAS has the potential to reconstruct parameters associated with ocean waves, and could ultimately facilitate their real-time estimation.

1 Introduction

Distributed Acoustic Sensing (DAS) instruments can provide highly sensitive measurements of various environmental physical fields at meter-resolutions along tens to hundreds of kilometers of optical fibers, like those embedded in telecommunication cables (Hartog, 2000; López-Higuera, 2002; Y. Li et al., 2021; Ip et al., 2023). Some of these physical fields include: acoustic wavefields (e.g. Rivet et al., 2021; Bouffaut et al., 2022; Wilcock et al., 2023), seismic wavefields (e.g. T. Dean et al., 2017a; H. F. Wang et al., 2018; Zhan, 2019; Jousset et al., 2022; Tonegawa et al., 2022) and temperature anomalies (e.g. Miller et al., 2018; Ide et al., 2021; Pelaez Quiñones et al., 2023).

In underwater environments, the possibility to describe various characteristics of surface gravity waves with DAS has also been exploited in previous works (Lindsey et al., 2019; Sladen et al., 2019; Williams et al., 2019; Guerin et al., 2022; Landrø et al., 2022; Williams et al., 2022; Xiao et al., 2022; Taweesintananon et al., 2023). In particular, Glover et al. (2023) presented empirical evidence of a correlation existing between seafloor DAS and wave-generated underwater pressure in coastal marine environments. Building upon these previous studies, our study focuses on: 1) reconstructing surface gravity wave heights

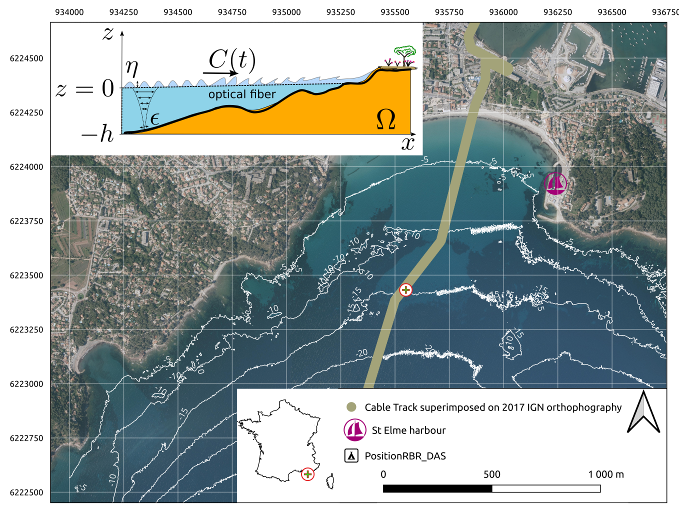

Figure 1. Aerial image of the bay of Les Sablettes (local coordinates). The isobaths in meters were extracted from the LITTO3D® PACA 2015 program. The position of the LSPM cable is indicated by the light ocre track and the RBR sensor by the cross and red circle marker. The top-left inset figure is a schematic description of the experiment as a function of depth with the main physical variables indicated.

from DAS measurements in a nearshore environment and 2) developing a theoretical formalism for comparing the energy associated with optical fiber deformation to the energy generated by surface gravity wave action at the sea bottom.

Our analysis, encompassing various sea-state conditions, shows that the response of DAS to the kinematics of nearshore surface gravity waves can be well approximated by the linear gravity wave theory. This implies, amongst others, that the nearshore wave spectrum can be inferred at high spatial resolution from DAS data. Additionally, we introduce a relationship to quantify the transfer function between the waves and the fiber.

2 Experimental setup for the DAS and pressure sensor

End of 2020, DAS and in situ pressure sea floor observations were collected in the bay of Les Sablettes, Saint-Mandrier-sur-Mer, in the South of France (Fig 1) ((Bouchette et al., 2023). A chirped-pulse ϕ-OTDR (phase-sensitive optical time-domain reflectometry) hDAS (High fidelity distributed acoustic sensor) interrogator (Pastor-Graells et al., 2016) providing measurements in strain units was connected to the land termination of the LSPM (Laboratoire Sous-marin Provence Méditerranée) seafloor cable (previously known as the MEUST-NumerEnv cable) (Sladen et al., 2019). This 50 km-long cable extends cross-shore from the coast to the bottom of the NW Mediterranean basin (Fig. 1). The acquisition was configured to sample every 10 m along the cable (same spatial sampling and gauge length) at 250 Hz. During the installation, the cable was buried 50 cm to 2 m deep along the first ∼500 m from the shoreline. Beyond that, the cable lays on the seafloor, as confirmed by visual surveys over the past 10 years.

Bottom hydraulic pressure data was sampled at 8 Hz between December 23, 2020 to January 6, 2021 with a RBR virtuoso^3 pressure sensor deployed at 15 m depth. The sensor was located about 1 km from the shoreline, next to an exposed cable section. To correct for dynamic pressure, atmospheric pressure measurements were retrieved from the

HTMNET station in Saint Elme Harbour (`https://htmnet.mio.osupytheas.fr/`), on the eastern edge of the bay (Fig. 1).

Swell propagation can be assumed to be nearly constant and close to aligned with the cable azimuth at the cable section of interest, where the colocated RBR sensor lies. This is a reasonable assumption considering the evenly-sloping bay configuration of Les Sablettes and its shallow water depths (∼15 m), meaning that swells are refracted along the cross-shore profile covered by the first few kilometers of cable.

3 Experimental analyses

In the following, we describe the empirical relationship between seafloor DAS and RBR pressure data and validate our ability to reconstruct ocean wave heights from DAS measurements, considering that the RBR pressure signal is known to convey reliable estimates.

3.1 Empirical relationship between seafloor DAS and pressure measurements

DAS strain time series in Figs. 2a,b, are highpassed at 10 mHz (with prior demeaning and tapering) for visualization to remove a non-stationary trend which is known to be fundamentally related to low-frequency temperature effects (e.g. Rathod et al., 1994; Fang et al., 2012; Ide et al., 2021). To match the sampling frequency of the pressure sensor (8 Hz), the DAS data were low-pass filtered and re-sampled (Fig. 2a).

The signal in Fig. 2b represents the raw pressure from the RBR sensor. Pressure-derived kh estimates ($k=$ angular wavenumber, $h=$ water depth) in Fig. 2c, indicate that the intermediate-depth wave regime assumption is reasonable over the whole time series. To quantitatively describe the transfer function between DAS strain and sea floor pressure, we focus our analysis on three different weather conditions: fair weather, light gale and moderate storm (Fig. 2). These weather conditions are identified from the seafloor pressure data and derived parameters, e.g. wave heights H_s and peak frequency f_p as detailed below (see Sec. 3.2).

Despite some similarities in the time series at the scale of the experiment (Figs. 2a,b), individual oscillations of the pressure and DAS signals show a clear mismatch in phase as depicted in Figure 3. This observed phase mismatch may arise from various factors such as the imperfect collocation of both sensors or the nature of the measurements: the pressure sensor provides local absolute measurements whereas DAS data are spatially differentiated measurements which has some consequences on the frequency content of the signals ((T. Dean et al., 2017b)). For these reasons, we move on with a spectral analysis.

Spectrograms of sea floor pressure and DAS strain signals (Fig. 2d,e) were computed over a 15-day period using 30-minutes non-overlapping windows. Different window durations (10, 20, 30 and 60 min) are tested to observe its influence on the results in Sec. 3.2. It can be seen that the DAS and RBR spectral density distributions are visually similar within the surface gravity wave band ($f \approx 0.04$ to 0.3 Hz, i.e. $T \approx 3$ to 25 s). Most of the surface gravity waves energy is clustered between 0.1 to 0.2 Hz. During the high-energy events, DAS records energy in the 0.2∼0.4 Hz frequency range which is not clearly captured by the RBR. Infragravity wave content ($f \lesssim 0.04$ Hz) on the RBR is minimal during the observation period, except during the storm on the 28th of Dec, where the DAS signals also shows clear infragravity energy. Infragravity wave activity appears recurrent on DAS for the observation period, but this may partially overlap with temperature-related signals.

Peak frequency time series, $f_p(t_w)$, was derived from pressure spectrograms within the surface gravity wave band ($f \approx 0.04$ to 0.3 Hz) for each time window, t_w. Subsequently,

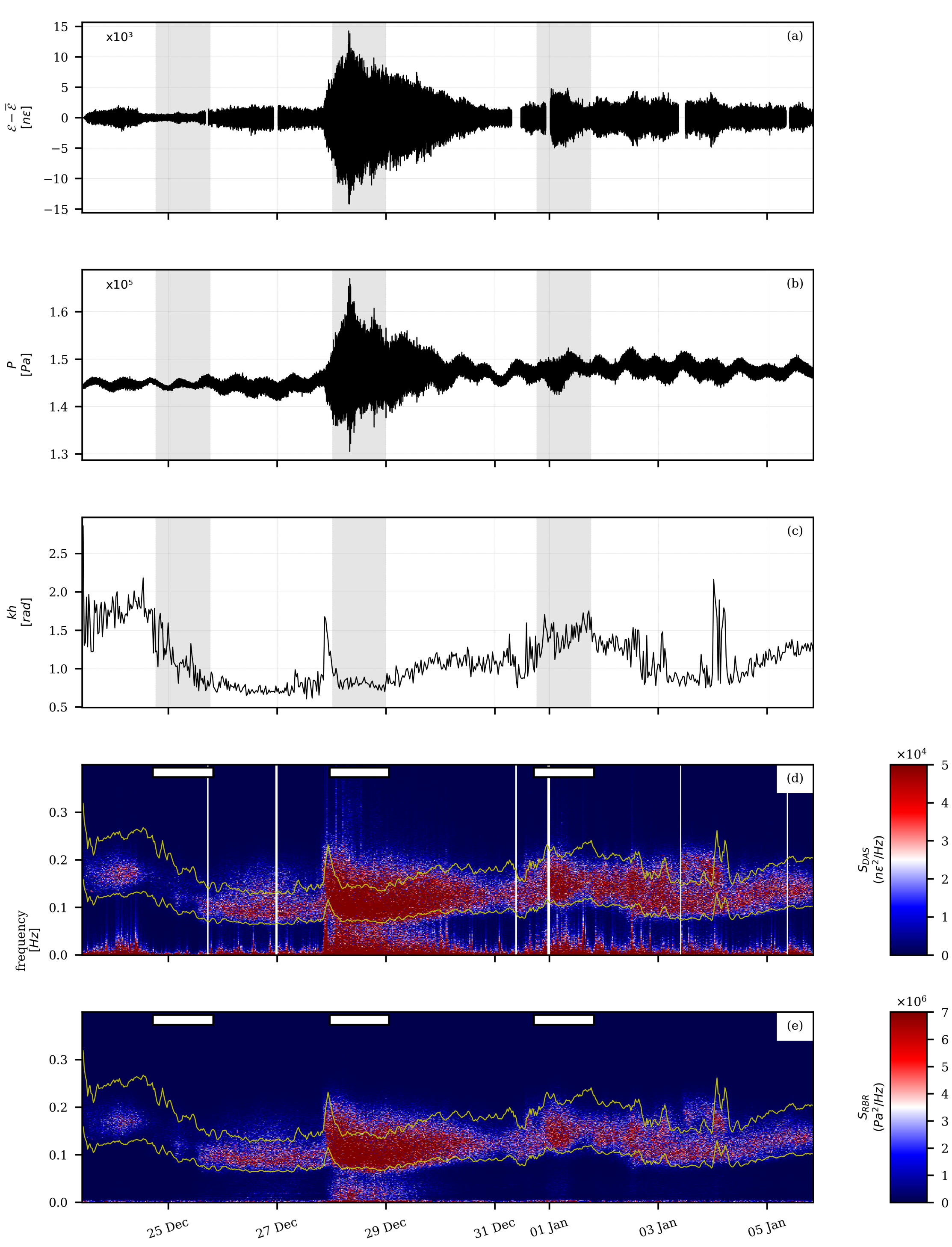

Figure 2. Time series of a) mean-centred and high-passed at 10 mHz (4-pole Butterworth filter) DAS signal, b) pressure sensor signal (P in Pa), and c) kh (in rad.) derived from the pressure sensor. The wave number k was calculated from the peak frequency using Eq. 7 (see section 4.1). d) Spectrogram of the DAS signal with outliers removed (white patches). e) Spectrogram of the pressure sensor signal. The frequency (f) integration limits ($1.5f_p$, $f_p/1.5$) are represented by yellow lines. Three selected periods (in chronological order i) fair-weather condition ii) storm condition, and iii) light gale condition), are represented by grey shaded boxes for a, b, c and in white patches on top of d, e.

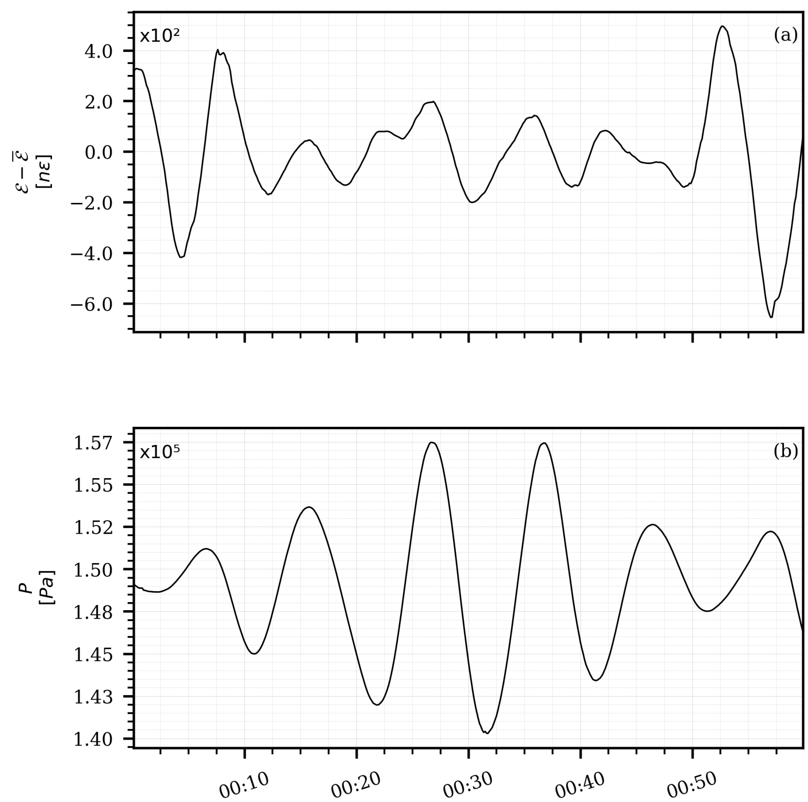

Figure 3. Time series of a) 1-min window mean-centred and high-passed at 10 mHz (4-pole Butterworth filter) of the 8 Hz DAS signal, b) 1-min window of the 8 Hz pressure sensor signal (P in Pa). The data starts at 12:00 28th of December 2020.

more accurate time-varying bounds for the surface gravity wave band were empirically estimated as $[f_p/1.5, f \times 1.5]$. These are superimposed onto spectrograms in Fig. 2d,e (yellow curves). The spectral energy E was then calculated by integrating the spectral density S within the time-variant wave band for both the RBR pressure sensor and the DAS measurement:

$$E(t_w) = \int_{f_p(t_w)/1.5}^{1.5 \cdot f_p(t_w)} S(f, t_w)\, df \tag{1}$$

Fig. 4 demonstrates a strong linear correlation between E_{DAS} and E_{RBR}. The coefficient of determination (R^2) for a 30-min window is 0.95, attesting to the robustness of the observed relationship. The black patches observed in Fig. 4 correspond to variable energy levels, ranging from low to high, in the specific weather conditions of fair-weather, light gale, and moderate storm. Other regressions, such as quadratic regression, were tested but were not optimal, underestimating the lowest energies, and are therefore not shown in Fig. 4.

Based on the aforementioned parameters, we obtain the following relationship for the linear regression between DAS and RBR spectral energies:

$$\begin{gathered} E_{RBR} = \beta\, E_{DAS} \\ \text{with } \beta = 93.86 \end{gathered} \tag{2}$$

The choice of frequency band for surface gravity waves has a relatively weak effect on the estimated average β value (as long as we remain within the range of gravity waves). For instance, a calculation boundary of $(2f_p,\ f_p/2)$ results in $\beta = 91.75$ ($R^2 = 0.95$). Fixed boundaries at (0.05, 0.3) Hz provided $\beta = 91.49$ ($R^2 = 0.95$).

3.2 Wave heights reconstruction from DAS measurements

Finally, using the β coefficient, it is possible to convert E_{DAS} from nanostrain^2 to Pa^2. Based on the linear theory, and taking an estimated cable depth of 14.6 m at the section of interest, we correct E_{DAS} for viscous attenuation at depth to get $E(t_w)_c = E(t_w)\frac{\cosh(k(h+z))}{\cosh(kh)}$. Then, we calculate the significant wave height, which can be directly derived from E_{DAS} following Horikawa (1988):

$$H_s(t_w) = 4\sqrt{E(t_w)_c} \tag{3}$$

Fig. 5a shows the time series of Hs calculated from the RBR pressure sensors and the DAS signal, while Fig. 5b summarizes different performance indicators of such procedure. This illustrates the remarkable accuracy of Hs estimates from DAS. Notably, for a 30-minute window, we achieve a coefficient of determination (R^2) of 0.95 and a Mean Absolute Percentage Error (MAPE) of 18.023, affirming excellent agreement between the estimated wave heights from both DAS and RBR.

4 Theoretical framework

So far, we have presented an empirical correlation between DAS and pressure sensor signals. In the following, we develop a formalism to describe this correlation physically, from the standpoint of gravity wave kinematics.

4.1 Conceptual model of cable - wave interactions

We start with a system Ω made of a water mass forced by waves coupled to a fiber cable coupled to the seabed as shown in Fig. 1, along which the wave-driven action remains spatially homogeneous. In the following, the physical quantities are given in a coordinate framework where the origin is at the still water level, z is positive upward, and x

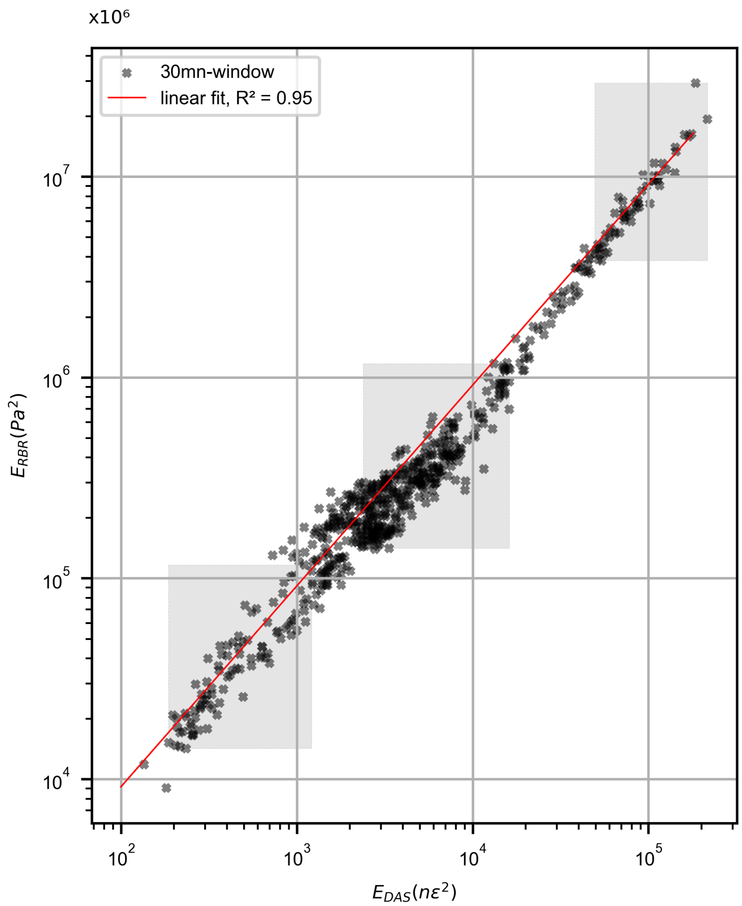

Figure 4. Bivariate correlation plot between the DAS and RBR pressure data. Best-fit linear (with zero y-intercept) is shown in continuous red. The three shaded boxes superimposed on the figure represent (from left-to-right): i) fair-weather condition ii) light gale condition and iii) storm condition.

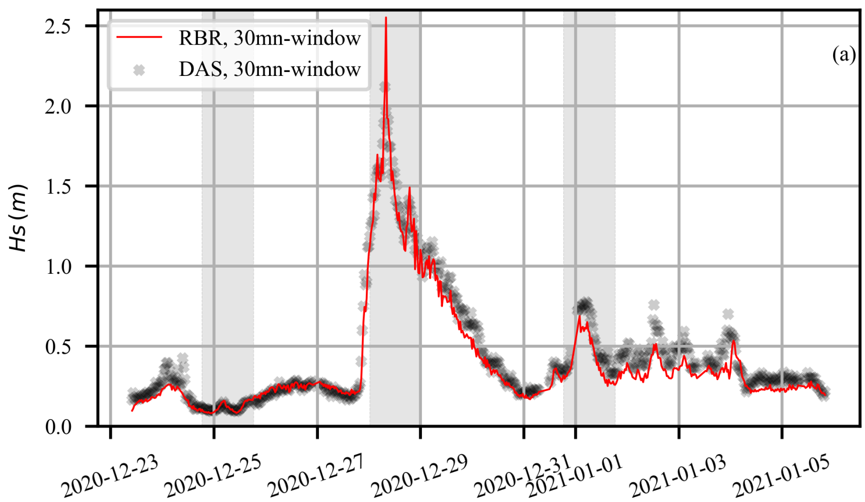

(b)

Window size (mn)	RMSE	MAE	R²	Error rate
10	0.008	0.063	0.94	18.308
20	0.007	0.06	0.949	17.816
30	0.006	0.06	0.95	18.023
60	0.007	0.061	0.947	18.917

Figure 5. a) Estimated wave height time series for DAS and RBR. Three selected shaded box were superimposed on the figure, representing i) fair-weather condition ii) storm condition and iii) light gale condition. On table b), error statistics are summarized as a function of window size (in mins). RMSE = root mean square error, MAE = mean absolute error, R^2 = coefficient of determination, Error Rate= mean absolute percentage error

positive landward (*i.e.* positive in the direction of wave propagation). In this setting, h is the mean water depth (a positive constant over time scales of the order of hours), $C(t)$ is the wave celerity, $u(x,z,t)$ and $w(x,z,t)$ are the instantaneous horizontal and vertical components of the water velocity, $p(x,z,t)$ is the instantaneous dynamic pressure of the water at depth z, $\tau(x,t)$ is the shear stress at the water-seabed interface driven by waves, $\mathbf{E}(x,t)$ is the ratio of deformation of the fiber cable per unit length along the cable (strain, a dimensionless unit).

To explore the relationship between DAS and pressure sensor signals, we consider the framework of the linear wave potential theory (Mei, 1992; R. G. Dean & Dalrymple, 1984). Following this assumption, we consider a velocity potential Φ on Ω that satisfies

$$\begin{cases} \Delta\Phi = \Phi_{xx} + \Phi_{zz} = 0 & \\ w = \phi_z = 0 & \text{at the sea bottom} \quad z = -h \\ (\Phi_t)_{z=0} = \frac{\partial \eta}{\partial t} & \text{Kinematic surface boundary condition} \\ (\Phi_t + g\eta)_{z=0} = C(t) & \text{Dynamic surface boundary condition} \end{cases} \tag{4}$$

where g is Earth's gravity. The set of Eqs. 4 forms a well-posed Laplace problem describing the evolution of a water mass forced by waves propagating over a horizontal rigid bottom at which fluid velocity nullifies. One solution for this system is:

$$\Phi(x,z,t) = \frac{ag}{\omega}\frac{\cosh k(h+z)}{\cosh kh} e^{(kx-\omega t)} \tag{5}$$

where a is the amplitude, $\omega = 2\pi/T = 2\pi f$ is the angular frequency (T being the period), and k the wave number of the propagating wave.

We assume also that wave quantities satisfy the surface gravity wave linear dispersion equation

$$\omega^2 = gk \tanh(kh) \tag{6}$$

which can be approximated following Guo (2002) by:

$$k = \frac{\omega^2}{g}(1 - e^{-(\omega^2 h/g)^{5/4}})^{2/5} \tag{7}$$

From the simple theoretical framework formed by Eqs. 4–7, we could derive most of the hydraulic quantities in Ω, including the dynamic pressure in the presence of waves $p = -\rho(gz - \Phi_t)$, where ρ is the density of water in [kg·m^{-3}]. However, we do not intend to relate instantaneous hydraulic quantities to the instantaneous deformation of the fiber cable directly. Instead, we relate the fiber cable strain $\mathbf{E}$ to the amplitude of some hydraulic quantities expressed at the sea bottom where the coupling occurs, assuming also that the physics are the same at any point along the abscissa axis in Ω. For designating such a transformation, we use capital letters in relation with the lowercase letter representing the physical quantity concerned (e.g. B for b, where b can be any wave parameter, such as pressure or orbital speed). Then we define the following operator:

$$B = \frac{1}{2}\left(\left|\max\left[b(x,z,t)|_{z=-h}\right]_{t\in\delta T}\right| + \left|\min\left[b(x,z,t)|_{z=-h}\right]_{t\in\delta T}\right|\right) \tag{8}$$

where δT is a time interval representative of some wave periods. The quantity B is homogeneous along the abscissa axis so that x can be removed from the formula.

Following this naming convention, we calculate three quantities: a) P^+, the amplitude of the excess of pressure at the sea bottom due to waves defined after the amplitude of the total pressure $P = \rho g h + P^+$; b) U_{orb} the amplitude of the horizontal component of orbital velocity oscillations at the sea bottom; c) X_{exc} the horizontal excursion of water particles at the sea bottom:

$$P^+ = \frac{\rho a g}{\cos(kh)} \tag{9}$$

$$U_{orb} = \frac{agk}{\omega \cosh(kh)} \tag{10}$$

$$X_{exc} = \frac{a}{\sinh(kh)} \tag{11}$$

The three equations above relate the properties of surface gravity waves to hydraulic quantities at the sea-bottom, but they cannot be directly related to the DAS measurements without also expressing the kinematic and dynamic conditions between the water at the sea-bottom and the sediment and fiber-optic cable.

4.2 Definition of the water - cable coupling

We examine the simple case where the horizontal motion of the water would drive the axial/longitudinal deformation of the fiber cable by simple shearing. If the fiber cable was perfectly coupled with the water (possibly through the seabed), X_{exc} would represent the amplitude of the longitudinal displacement of the fiber cable during a wave length. The deformation of the fiber would be defined by the ratio $X_{exc}k/2\pi$ for a gauge length (10 m), which is smaller than the wavelength. Obviously, in such a case, the fiber deformation would be by far beyond its elastic behavior; in practice, only a small amount of the water deformation – let us say a ratio α – may be transmitted to the fiber cable. $\mathbf{E}$ could then be written after this ratio α and X_{exc} :

$$\mathbf{E} = \frac{\alpha k a}{2\pi \sinh(kh)} \tag{12}$$

5 Deriving a more physically-informed expression of the coefficient β

Using field measurements, we have shown that there is a linear relationship by an empirical factor β (from Eq. 2, here renamed β_e), between the power spectral magnitude of the deformation of the fiber $\mathbf{E}$ (in nanostrain^2) and that of the excess pressure (in Pa^2) induced at the ocean bottom by the propagating waves:

$$(P^+)^2 = \beta_e \mathbf{E}^2 \tag{13}$$

The previously derived equations allow us to derive a similar expression based on linear wave theory since P^+ on the sea-bottom is linked to surface gravity waves via Eq. 9, and to the DAS measurement via Eq. 12

$$\mathbf{E} = \alpha \frac{P^+ k}{2\pi \rho g \tanh(kh)} \tag{14}$$

Based on Eq. 14, we can evaluate α. For the peak storm (the 28th of December at 8:00, see Fig. 2), the peak period is $T_p = 10.6$ s. We take the cable depth $h = 14.6$ m in a water of mean density $\rho = 1028$ kg/m^3. From Eq. 9, the estimated excess of pressure for a wave of amplitude $a = H_s/2 \approx 1.2$ m (from Fig. 5) is $P^+ \approx 9.1$ kPa. From all these values, we can anticipate that the parameter α would be on the order of 1.2×10^{-4}.

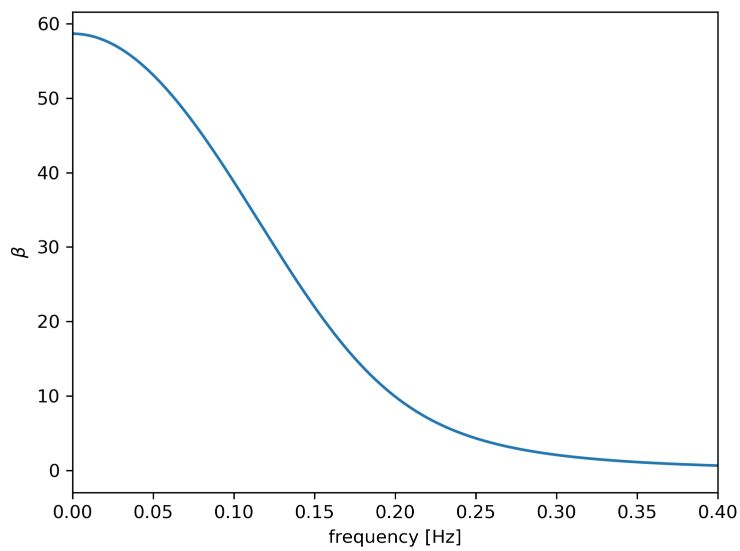

Figure 6. β as a function of frequency from Eq. 16 , using h =14.6 m, ρ = 1028 kg/m^3 and assuming a constant α value of 1.2×10^5 (estimated following Eq. 14 as in the Discussion section, with DAS in nanostrain units)

Squaring Eq. 14, we can extract a modeled β factor (β_m)

$$\beta_m = \frac{1}{\alpha^2} \frac{4\pi^2 \rho^2 g^2 \tanh^2(kh)}{k^2} \tag{15}$$

Using the dispersion relation (Eq. 6), we obtain a new relationship for β_m :

$$\begin{aligned} \beta_m &= \frac{1}{\alpha^2 \gamma^2} \\ \text{with } \gamma &= \frac{1}{2\pi\rho C^2} \end{aligned} \tag{16}$$

We can compare the empirical β_e coefficient estimated from windowed linear regressions of the spectral energy of strain and pressure with a modelled β_m derived from Eq. 16. α is retrieved from Eq. 14 by taking P^+ and $\mathbf{E}$ from the data, while γ is derived from $C = (kT_p)^{-1}$, where k is estimated from T_p via Eq. 7. The relationship between the empirical and modeled β is illustrated in Fig. 7a, b for 5mn and 30mn-window analysis. Although the linear relationship captures only a limited fraction of the variability in the data ($R^2 = 0.58$ for 5m-window and $R^2 = 0.53$ for 30m-window) , most points are clustered around the identical function, demonstrating a substantial degree of agreement between the two β values. This evidently supports the applicability of the linear theory to describe the energy transfer mechanism from surface gravity waves into the cable. From Eq. 16, it is suggested that β is frequency-dependent, which may explain its window-wise variability. This is confirmed by the clustered distribution of the peak period in Fig. 7b, which shows that β values are proportional to wave period, in agreement with Eq. 16. As a confirmation of this relationship, Fig. 6 illustrates β as a function of wave frequency for a given set of parameters.

Time series of the distribution of empirical and modeled β values over time for 30-min spectral energy windowing confirms the agreement between both estimates (Fig. 7c).

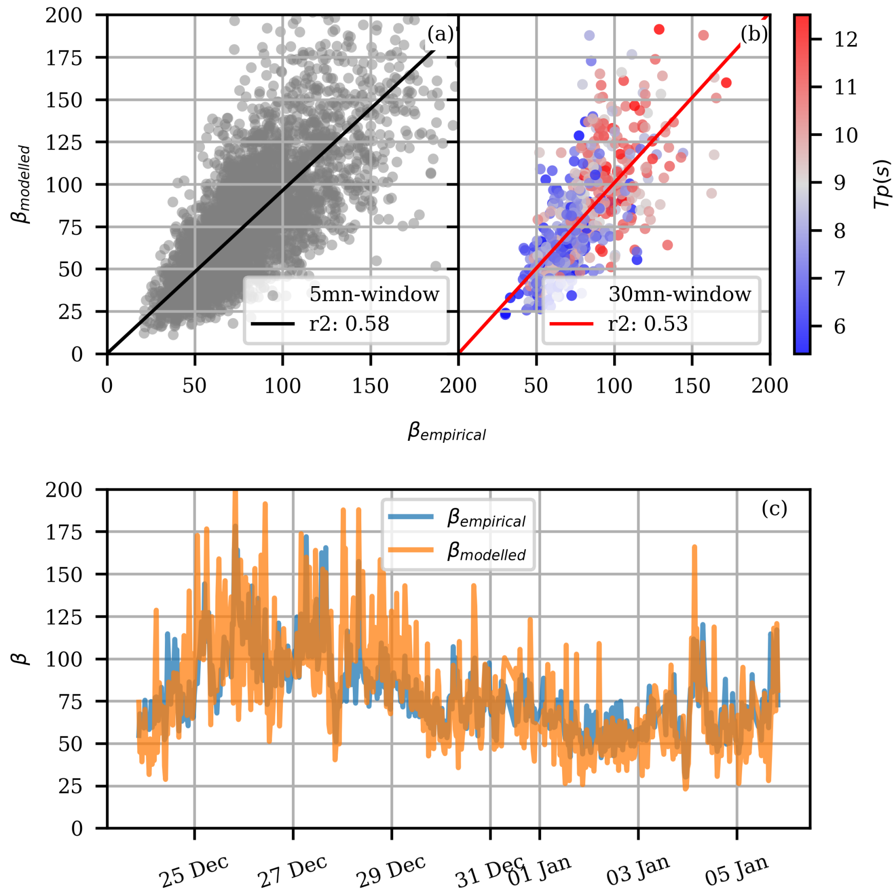

Figure 7. Bivariate correlation plot between empirical and modeled β (a) for 5-min spectral energy estimates and (b) for 30-min estimates as a function of the peak period (Tp (s)). Best-fit linear (with zero y-intercept) is shown in continuous red. Note that the best linear fit nearly matches the identical function (x = y). The lower panel (c) depicts the temporal distribution of the scatter in (b).

From Eq. 16, it appears that the transfer coefficient between the wave pressure signal and the DAS strain signal β is characterised by two parameters: γ, which can be considered the fluid- or wave-related factor. This term represents the kinematics of the water oscillations that causes the cable deformation; and α, which represents both, the fraction of wave displacements that is effectively transmitted into the fiber and the dynamic response of the fiber, i.e. a superposition of physical conditions related to the structural and material characteristics of the cable, its coupling nature to the seabed, and the specific visco-elastic mechanism(s) of stress transfer from the fluid into the cable. At this stage, it remains challenging to separate these different effects, but we stress that the α parameter is subject to further parameterization and decomposition based on more advanced dynamic and elasto-mechanical considerations, as well as more detailed observations.

6 Discussion

We have established a correlation between cable deformation and wave-induced pressure that can be sufficiently described kinematically. However, such correlation with pressure is not necessarily causal, as the specific mechanisms transferring stresses from the water into the fiber are not fully constrained. Pressure-induced Poisson effect on the cable and/or seabed bending/compliance are both often considered to participate in the fiber deformation. For instance, previous studies have attributed the observation of surface gravity waves to direct dynamic pressure loading (e.g. Glover et al., 2023; Taweesintananon et al., 2023). However, the linear wave theory predicts similar depth-dependent functions and oscillation patterns for both, the wave-induced dynamic pressure and the horizontal component of the orbital acceleration motions. The latter could exert important shear stresses via boundary layer-seabed friction and/or via differential shearing of the cable structure, which could in turn cause axial fiber elongation. The second mechanism may be less significant, considering the high shear modulus of silica ($\sim 10^9$ Pa) (López-Higuera, 2002). However, the shear modulus of silicon coatings can be as low as $\sim 10^6$ Pa (D. Li et al., 2012; H. Wang et al., 2018), while dynamic wave pressure values at the seafloor are generally much larger than its corresponding shear stresses. For instance, the estimated maximum excess pressure during the peak storm as previously estimated from Eq. 14 is $\sim$9.1 kPa, while based on Eq. 10, the maximum shear stress $\tau = \frac{1}{2}\rho f_w U_{orb}^2$ for a typical seabed friction coefficient f_w of 0.1 (Hardisty, 1990; You & Yin, 2007) is estimated around 33 Pa for the same wave (330 Pa for a relatively high $f_w = 1$). On the other hand, considering the predominantly axial strain sensitivity of optical fibers (Kuvshinov, 2016; Papp et al., 2017), it may still occur that the deformations effectively transferred near-axial shear stresses on the fiber are as relevant or perhaps even more so than those induced by (mostly broadside) dynamic pressure loading. In the case of a sloping seabed, axial dynamic pressure gradients could also develop that potentially induce cable deformations in the form of shear stresses. Additionally, the asymmetry of more realistic, non-sinusoidal nearshore gravity waves is expected to increase seabed shear stresses (Gonzalez-Rodriguez & Madsen, 2007). Further analyses are required in order to reliably quantify and assess the pressure loading, seafloor compliance and frictional contributions to fiber deformation.

Although the coupling of optical fibers to different host structures (e.g. cables with coating, armoring) and that of cables to seabeds with variable materials and fabrics (e.g. sediments, rocks, seagrass) is implicit in the α parameter, the specific ranges of validity and the stability of our transfer function under extreme conditions remain unexplored. For instance, a considerable cable burial degree is expected to attenuate the gravity wave forces, while extreme variations in wave amplitude or direction may influence the transfer function non-linearly. However, no clear saturation effects were observed in the DAS signal during the most energetic storm event, even at high frequencies. This suggests that the high non-linearity of surface waves in a nearshore environment does not compromise the reliability of DAS measurements nor the transfer function. However, it should be noted that this has yet to be confirmed for much harsher wave conditions, such as those present during a hurricane.

7 Conclusion

In this study, we have presented a methodology to construct a simple transfer function between nearshore surface gravity waves and the induced DAS strain on a seafloor fiber optic cable in the frequency band ∼0.04-0.3 Hz and under diverse sea-state conditions. The linear potential wave theory is sufficient to describe the main characteristics of the transfer function from a kinematic standpoint, including its frequency-dependence. Our theoretical development also highlights the possibility to quantify the relative contribution of waves and of the cable in this transfer function. The latter currently remains an empirical parameter that could be further decomposed based on more advanced, e.g. dynamical, considerations. This reaffirms the major potential of seafloor DAS as a tool for the reconstruction of the nearshore gravity wave spectrum along seafloor cables with spatial resolutions of a few meters.

Additional experimental steps are required to verify the potential dependency of such transfer function (more specifically the α parameter) on cable environment (depth, burial, cable type/integrity) as well as its robustness under an even wider range of swell environments (kh, H_s). The sensitivity, high resolution, and wide coverage of DAS technology opens up a vast field of ocean research and practical applications, which in addition to the retrieval of significant wave heights as shown in this study, suggests the possibility of extracting and quantifying more complex wave propagation characteristics.

References

Bouchette, F., Sladen, A., Meulé, S., & Pelaez-Quinones, J. (2023). *Das and pressure sensor datasets for the reconstruction of nearshore surface gravity wave spectrum from distributed acoustic sensing time series [dataset].* OSU OREME. Retrieved from https://data.oreme.org/doi/view/7d5e2f17-bad6-4ac3-87e2-84888d0d6699 doi: 10.15148/7d5e2f17-bad6-4ac3-87e2-84888d0d6699

Bouffaut, L., Taweesintananon, K., Kriesell, H. J., Rørstadbotnen, R. A., Potter, J. R., Landrø, M., … et al. (2022). Eavesdropping at the Speed of Light: Distributed Acoustic Sensing of Baleen Whales in the Arctic. *Frontiers in Marine Science*, *9*. doi: 10.3389/fmars.2022.901348

Dean, R. G., & Dalrymple, R. (1984). *Water wave mechanics for engineers and scientists.* (Prentice Hall ed.).

Dean, T., Cuny, T., & Hartog, A. H. (2017a). The effect of gauge length on axially incident P-waves measured using fibre optic distributed vibration sensing. *Geophysical Prospecting*, *65*(1), 184-193. doi: https://doi.org/10.1111/1365-2478.12419

Dean, T., Cuny, T., & Hartog, A. H. (2017b, 1). The effect of gauge length on axially incident p-waves measured using fibre optic distributed vibration sensing. *Geophysical Prospecting*, *65*, 184-193. Retrieved from https://onlinelibrary.wiley.com/doi/full/10.1111/1365-2478.12419https://onlinelibrary.wiley.com/doi/abs/10.1111/1365-2478.12419https://onlinelibrary.wiley.com/doi/10.1111/1365-2478.12419 doi: 10.1111/1365-2478.12419

Fang, Z., Chin, K. K., Cai, H., & Qu, R. (2012). Fundamentals of Optical Fiber Sensors. In (p. 96-97). John Wiley & Sons, Ltd. doi: 10.1002/9781118381717.ch3

Glover, H., Wengrove, M. E., & Holman, R. (2023). Distributed acoustic sensing of nearshore processes in Duck, NC, USA. In *Coastal sediments 2023* (p. 1576-1583). doi: 10.1142/9789811275135_0146

Gonzalez-Rodriguez, D., & Madsen, O. S. (2007). Seabed shear stress and bedload transport due to asymmetric and skewed waves. *Coastal Engineering*, *54*(12), 914-929. doi: 10.1016/j.coastaleng.2007.06.004

Guerin, G., Rivet, D., van den Ende, M., Stutzmann, E., Sladen, A., & Ampuero, J. P. (2022). Quantifying microseismic noise generation from coastal reflection of gravity waves recorded by seafloor DAS. *Geophysical Journal International*, *231*. doi: 10.1093/gji/ggac200

Guo, J. (2002). Simple and explicit solution of wave dispersion equation. *Coastal Engineering*, *45*, 71-74.

Hardisty, J. (1990). *Beaches: Form and processes* (London: Unwin Hyman ed.).

Hartog, A. (2000). Distributed fiber-optic sensors: principles and applications. In *Optical fiber sensor technology* (pp. 241–301). Springer. doi: 10.1007/978-1-4757-6079-8_4

Horikawa, K. (1988). Nearshore dynamics and coastal processes: Theory, measurement, and predictive models. *Tokyo : University of Tokyo Press*, 522.

Ide, S., Araki, E., & Matsumoto, H. (2021). Very broadband strain-rate measurements along a submarine fiber-optic cable off Cape Muroto, Nankai subduction zone, Japan. *Earth Planets Space*, *73*(63). doi: 10.1186/s40623-021-01385-5

Ip, E., Huang, Y.-K., Huang, M.-F., Yaman, F., Wellbrock, G., Xia, T., ... Aono, Y. (2023). Das over 1,007-km hybrid link with 10-tb/s dp-16qam co-propagation using frequency-diverse chirped pulses. *Journal of Lightwave Technology*, *41*(4), 1077-1086. doi: 10.1109/JLT.2022.3219369

Jousset, P., Currenti, G., Schwarz, B., Chalari, A., Tilmann, F., Reinsch, T., ... Krawczyk, C. (2022). Fibre optic Distributed Acoustic Sensing of volcanic events. *Nature Communications*, *13*. doi: 10.1038/s41467-022-29184-w

Kuvshinov, B. (2016). Interaction of helically wound fibre-optic cables with plane seismic waves. *Geophysical Prospecting*, *64*(3), 671-688. doi: 10.1111/1365-2478.12303

Landrø, M., Bouffaut, L., Kriesell, H. J., Potter, J. R., Rørstadbotnen, R. A., Taweesintananon, K., ... Storvik, F. (2022). Sensing whales, storms, ships and earthquakes using an Arctic fibre optic cable. *Sci Rep*, *12*(19226). doi: 10.1038/s41598-022-23606-x

Li, D., Ren, L., & Li, H. (2012). Mechanical property and strain transferring mechanism in optical fiber sensors. In M. Yasin, S. W. Harun, & H. Arof (Eds.), *Fiber optic sensors* (chap. 18). Rijeka: IntechOpen. doi: 10.5772/27731

Li, Y., Karrenbach, M., & Ajo-Franklin, J. B. (2021). A Literature Review: Distributed Acoustic Sensing (DAS) Geophysical Applications Over the Past 20 Years. *Distributed Acoustic Sensing in Geophysics: Methods and Applications*, 229–291. doi: 10.1002/9781119521808.ch17

Lindsey, N. J., Dawe, T. C., & Ajo-Franklin, J. B. (2019). Illuminating seafloor faults and ocean dynamics with dark fiber Distributed Acoustic Sensing. *Science*, *366*(6469), 1103-1107. doi: 10.1126/science.aay5881

López-Higuera, J. M. (Ed.). (2002). *Handbook of Optical Fibre Sensing Technology* (1st ed.). John Wiley & Sons, ltd.

Mei, C. C. (1992). The Applied Dynamics of Ocean Surface Waves. In *Advanced series on ocean engineering: Volume 1.* World Scientific. doi: 10.1142/0752

Miller, D. E., Coleman, T., Zeng, X., Patterson, J. R., Reinisch, E. C., Cardiff, M. A., ... Thurber, C. H. (2018). DAS and DTS at Brady Hot Springs: Observations about coupling and coupled interpretations. In *Proceedings of the 43rd workshop on geothermal reservoir engineering, stanford, ca, usa* (pp. 12–14).

Papp, B., Donno, D., Martin, J. E., & Hartog, A. H. (2017). A study of the geophysical response of distributed fibre optic acoustic sensors through laboratory-scale experiments. *Geophysical Prospecting*, *65*(5), 1186-1204. doi: 10.1111/1365-2478.12471

Pastor-Graells, J., Martins, H., Garcia-Ruiz, A., Martin-Lopez, S., & Gonzalez-Herraez, M. (2016). Single-shot distributed temperature and strain tracking using direct detection phase-sensitive OTDR with chirped pulses. *Optics express*, *24*(12), 13121–13133. doi: 10.1364/OE.24.013121

Pelaez Quiñones, J., Sladen, A., Ponte, A., Lior, I., Ampuero, J.-P., Rivet, D., ... Coyle, P. (2023). High resolution seafloor thermometry for internal wave and upwelling monitoring using distributed acoustic sensing. *Sci Rep*, *13*, 17459. doi: 10.1038/s41598-023-44635-0

Rathod, R., Pechstedt, R. D., Jackson, D. A., & Webb, D. J. (1994). Distributed temperature-change sensor based on Rayleigh backscattering in an optical fiber. *Optics letters*, *19*(8), 593-595.

Rivet, D., de Cacqueray, B., Sladen, A., Roques, A., & Calbris, G. (2021). Preliminary assessment of ship detection and trajectory evaluation using Distributed Acoustic Sensing on an optical fiber telecom cable. *The Journal of the Acoustical Society of America*, *149*(4), 2615-2627. doi: 10.1121/10.0004129

Sladen, A., Rivet, D., Ampuero, J. P., Barros, L., Hello, Y., Calbris, G., & Lamare, P. (2019). Distributed sensing of earthquakes and ocean-solid Earth interactions on seafloor telecom cables. *Nature Communications*, *10*, 5777. doi: 10.1038/s41467-019-13793-z

Taweesintananon, K., Landrø, M., Potter, J. R., Johansen, S. E., Rørstadbotnen, R. A., Bouffaut, L., ... Storvik, F. (2023). Distributed acoustic sensing of ocean-bottom seismo-acoustics and distant storms: A case study from Svalbard, Norway. *Geophysics*, *88*(3), B135-B150. doi: 10.1190/geo2022-0435.1

Tonegawa, T., Araki, E., Matsumoto, H., Kimura, T., Obana, K., Fujie, G., ... Kodaira, S. (2022). Extraction of P Wave From Ambient Seafloor Noise Observed by Distributed Acoustic Sensing. *Geophysical Research Letters*, *49*(4), e2022GL098162. doi: https://doi.org/10.1029/2022GL098162

Wang, H., Jiang, L., & Xiang, P. (2018). Improving the durability of the optical fiber sensor based on strain transfer analysis. *Optical Fiber Technology*, *42*, 97-104. doi: 10.1016/j.yofte.2018.02.004

Wang, H. F., Zeng, X., Miller, D. E., Fratta, D., Feigl, K. L., Thurber, C. H., & Mellors, R. J. (2018). Ground motion response to an ML 4.3 earthquake using co-located distributed acoustic sensing and seismometer arrays. *Geophysical Journal International*, *213*(3), 2020-2036. doi: 10.1093/gji/ggy102

Wilcock, W. S. D., Abadi, S., & Lipovsky, B. P. (2023). Distributed acoustic sensing recordings of low-frequency whale calls and ship noise offshore Central Oregon. *JASA Express Letters*, *3*(2), 026002. doi: 10.1121/10.0017104

Williams, E. F., Fernández-Ruiz, M. R., Magalhaes, R., Vanthillo, R., Zhan, Z., González-Herráez, M., & Martins, H. (2019). Distributed sensing of microseisms and teleseisms with submarine dark fibers. *Nature Communications*, *10*. doi: 10.1038/s41467-019-13262-7

Williams, E. F., Zhan, Z., Martins, H. F., Fernández-Ruiz, M. R., Martín-López, S., González-Herráez, M., & Callies, J. (2022). Surface Gravity Wave Interferometry and Ocean Current Monitoring With Ocean-Bottom DAS. *Journal of Geophysical Research: Oceans*, *127*(5), e2021JC018375. doi: 10.1029/2021JC018375

Xiao, H., Tanimoto, T., Spica, Z. J., Gaite, B., Ruiz-Barajas, S., Pan, M., & Viens, L. (2022). Locating the Precise Sources of High-Frequency Microseisms Using Distributed Acoustic Sensing. *Geophysical Research Letters*, *49*(17), e2022GL099292. doi: https://doi.org/10.1029/2022GL099292

You, Z.-J., & Yin, B. (2007). Direct measurement of bottom shear stress under water waves. *Journal of Coastal Research SI 50 (Proceedings of the 9th International Coastal Symposium)*, 1132 – 1136.

Zhan, Z. (2019). Distributed Acoustic Sensing Turns Fiber-Optic Cables into Sensitive Seismic Antennas. *Seismological Research Letters*, *91*(1), 1-15. doi: 10

.1785/0220190112

Acronyms

DAS Distributed Acoustic Sensing

8 Open Research

The DAS dataset was recorded on the seafloor LSPM (Laboratoire Sous-marin Provence Méditerranée) cable south of Toulon, which was part of the Mediterranean Eurocentre for Underwater Sciences and Technologies (MEUST) infrastructure at the time of acquisition (see Sladen et al. (2019) for details) using an Aragón Photonics hDAS interrogator. MEUST is financed with the support of the CNRSIN2P3, the Region Sud, France (CPER the State (DRRT), and FEDER.

The datasets for Distributed Acoustic Sensing (DAS) and pressure sensor data used in the reconstruction of nearshore surface gravity wave spectrum from DAS time series are accessible at `https://doi.org/10.15148/7d5e2f17-bad6-4ac3-87e2-84888d0d6699`

Data processing and analyses largely relied on Python libraries: SciPy (`https://scipy.org/`), NumPy (`https://numpy.org/`), Pandas (`https://pandas.pydata.org/`), Matplotlib (`https://matplotlib.org/`), Dask (https://www.dask.org/) and h5Py (`https://www.h5py.org/`).

Acknowledgments

We are grateful to GLADYS (`https://www.gladys-littoral.org/`) for the water pressure sensors deployed at the field site Les Sablettes and for all the logistics and funding for the deployment (boat, scuba diving equipment,...). The HTMNET programm (`https://htmnet.mio.osupytheas.fr`) provided us the atmospheric data. This project has received financial support from the CNRS through the MITI interdisciplinary programs through its exploratory research program. J.P.Q. was supported by the SEAFOOD project, funded by grant ANR-17-CE04-0007 of the French Agence Nationale de la Recherche, Université Côte d'Azur IDEX program UCA^{JEDI} ANR-15-IDEX-0001, and the Doeblin Federation (FR2800 CNRS), and the project MARMOR, funded by ANR-21-ESRE-0020 of the France 2030 program of the French Agence Nationale de la Recherche.

Figure1.

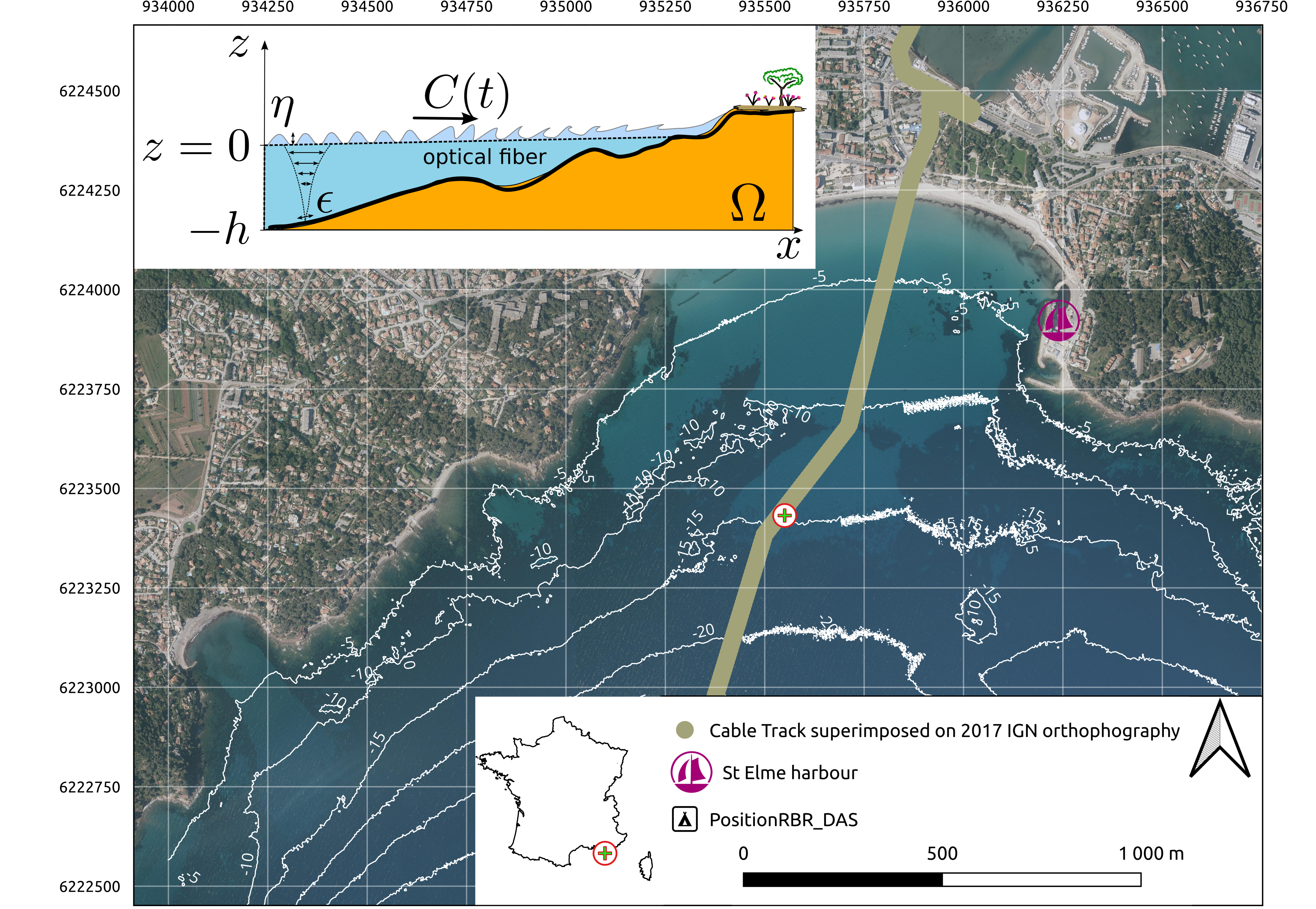

934000
934250
934500
934750
935000
935250
935500
935750
936000
936250
936500
936750
6224500
6224250
6224000
6223750
6223500
6223250
6223000
6222750
6222500
z
η
$C(t)$
$z = 0$
optical fiber
ϵ
Ω
$-h$
x
Cable Track superimposed on 2017 IGN orthophography
St Elme harbour
PositionRBR_DAS
0
500
1 000 m

Figure2.

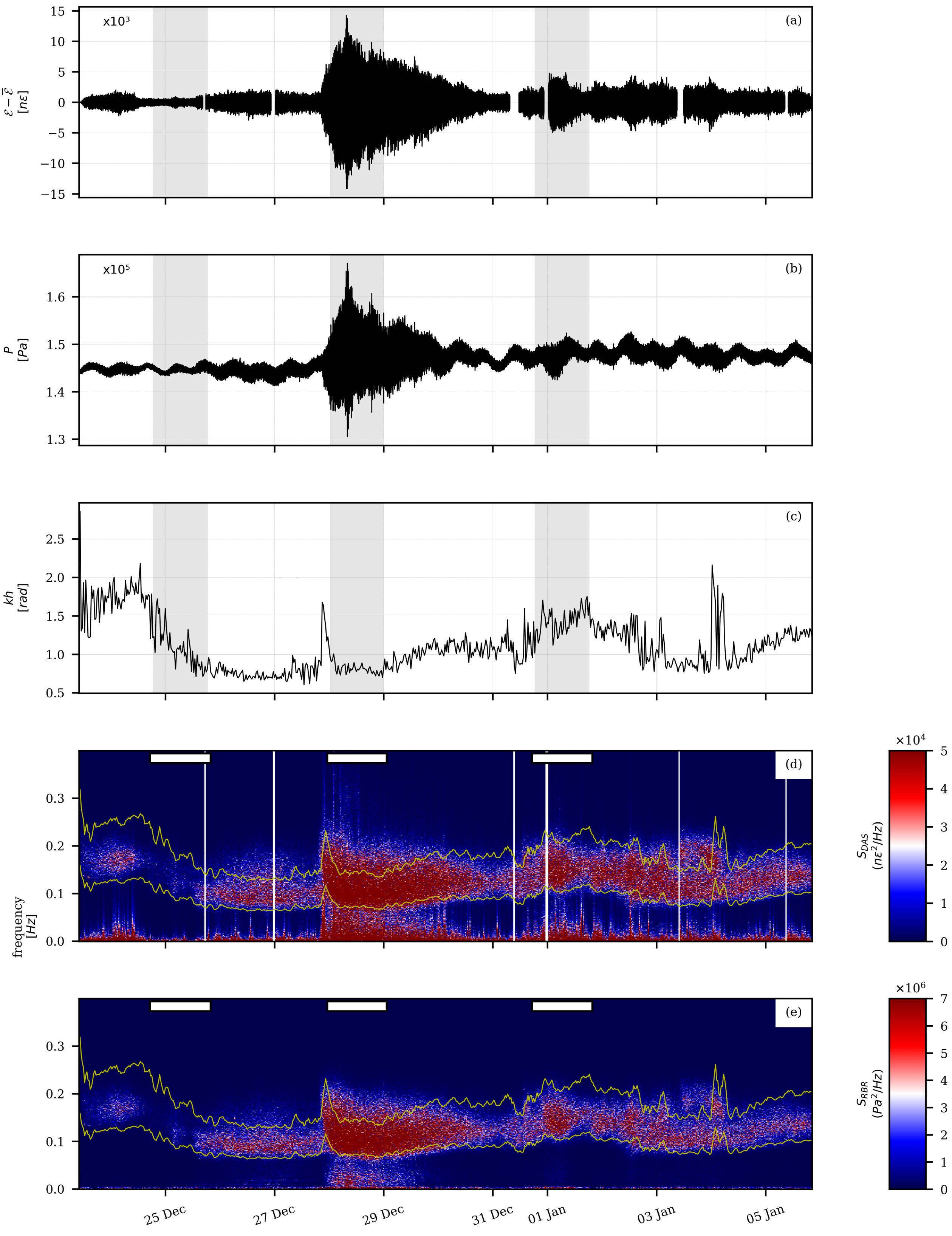

x10³
(a)
$\mathcal{E}-\overline{\mathcal{E}}$ [$n\varepsilon$]
x10⁵
(b)
P [Pa]
(c)
kh [rad]
(d)
frequency [Hz]
×10⁴
S_{DAS} ($n\varepsilon^2/Hz$)
(e)
×10⁶
S_{RBR} (Pa^2/Hz)
25 Dec
27 Dec
29 Dec
31 Dec
01 Jan
03 Jan
05 Jan

Figure3.

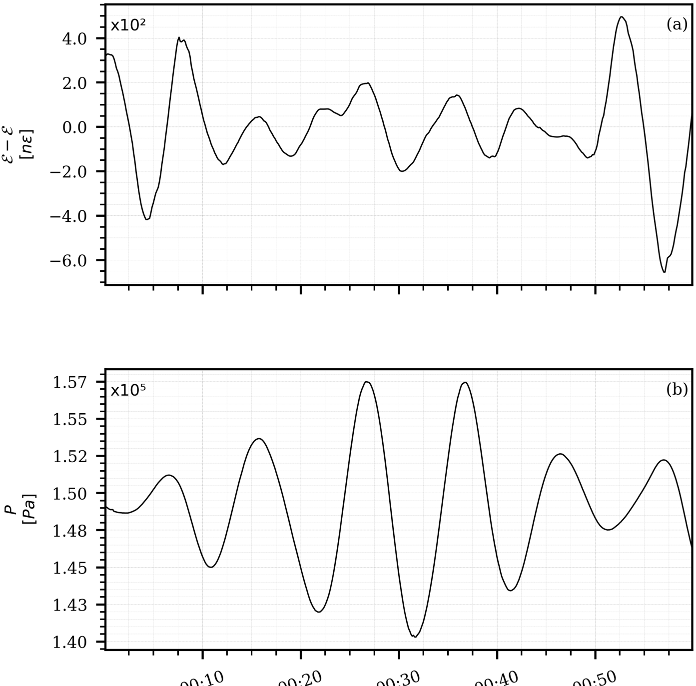

x10²
(a)
4.0
2.0
0.0
−2.0
−4.0
−6.0
$\mathcal{E} - \overline{\mathcal{E}}$
[$n\varepsilon$]
x10⁵
(b)
1.57
1.55
1.52
1.50
1.48
1.45
1.43
1.40
P
[Pa]
00:10
00:20
00:30
00:40
00:50

Figure4.

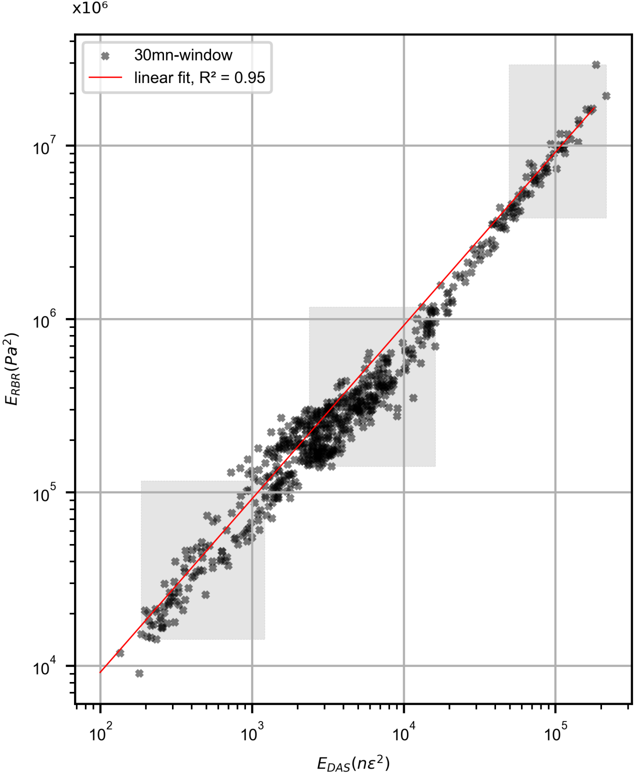

x10⁶
30mn-window
linear fit, R² = 0.95
10^7
10^6
10^5
10^4
$E_{RBR}(Pa^2)$
10^2
10^3
10^4
10^5
$E_{DAS}(n\varepsilon^2)$

Figure5.

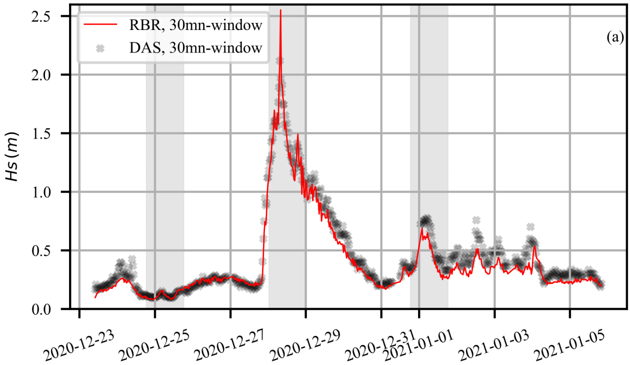

(b)

Window size (mn)	RMSE	MAE	R^2	Error rate
10	0.008	0.063	0.94	18.308
20	0.007	0.06	0.949	17.816
30	0.006	0.06	0.95	18.023
60	0.007	0.061	0.947	18.917

Figure6.

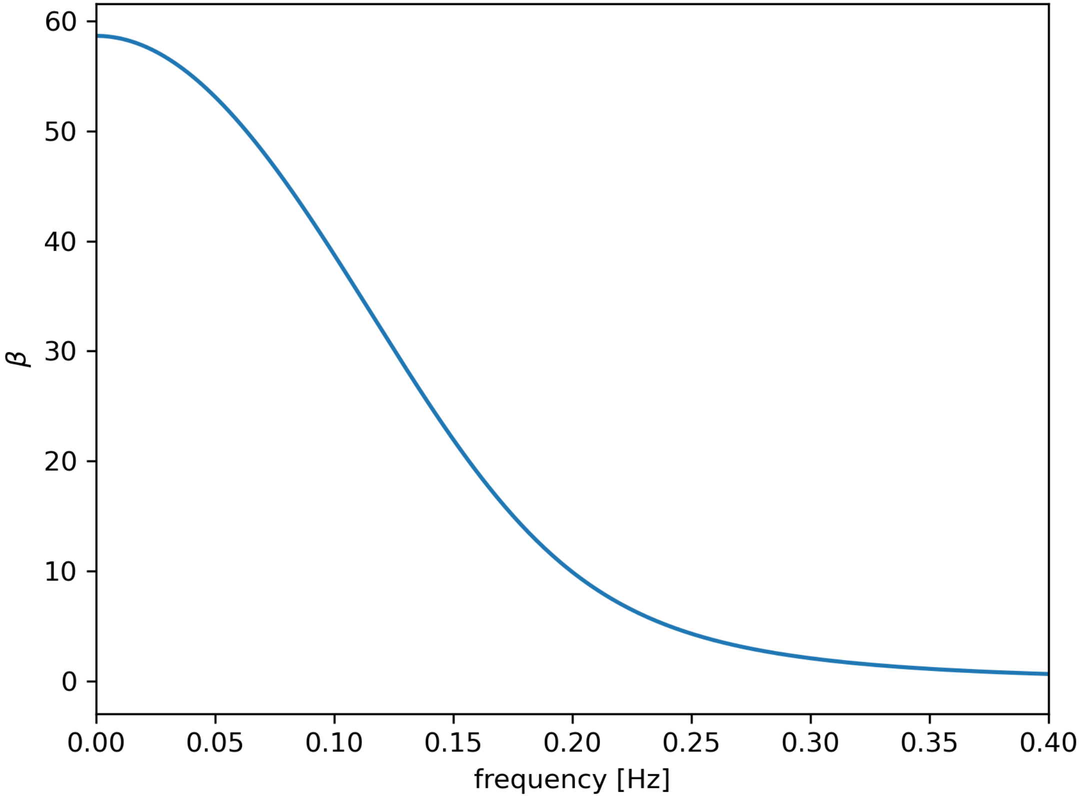

60
50
40
30
20
10
0
β
0.00
0.05
0.10
0.15
0.20
0.25
0.30
0.35
0.40
frequency [Hz]

Figure7.

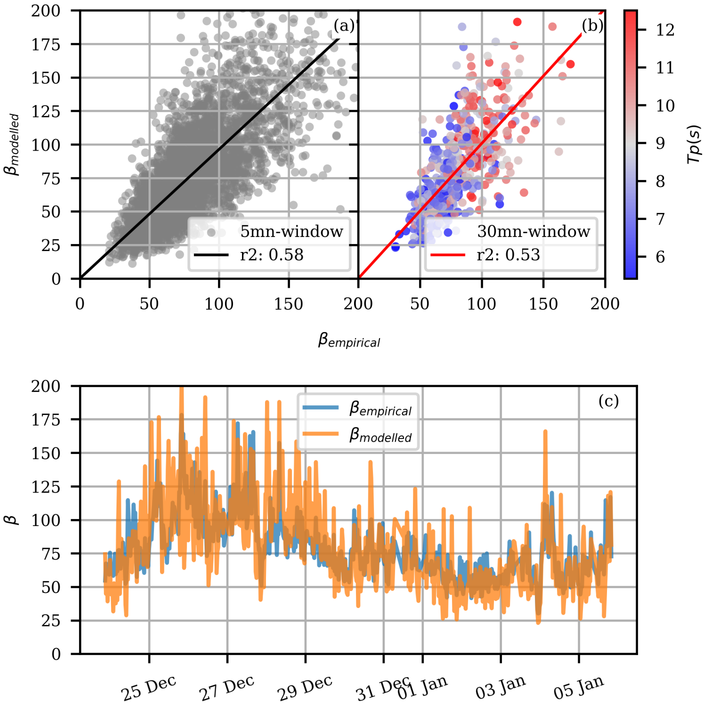

(a)
(b)
5mn-window
r2: 0.58
30mn-window
r2: 0.53
$\beta_{modelled}$
$\beta_{empirical}$
$Tp(s)$
(c)
$\beta_{empirical}$
$\beta_{modelled}$
β
25 Dec
27 Dec
29 Dec
31 Dec
01 Jan
03 Jan
05 Jan